Journal of Computational Physics 322 (2016) 309–325

Contents lists available at ScienceDirect

Journal of Computational Physics

www.elsevier.com/locate/jcp

Boundary Variation Diminishing (BVD) reconstruction: A new approach to improve Godunov schemes

Ziyao Sun, Satoshi Inaba, Feng Xiao *

Department of Mechanical Engineering, Tokyo Institute of Technology, 4259 Nagatsuta Midori-ku, Yokohama, 226-8502, Japan

ARTICLE INFO

Article history:
Received 4 February 2016
Received in revised form 28 June 2016
Accepted 28 June 2016
Available online 5 July 2016

Keywords:
Finite volume method
Godunov method
Discontinuity
Reconstruction
Boundary Variation Diminishing (BVD)
WENO
THINC
Riemann solver
Compressible flow
Shock wave

ABSTRACT

This paper presents a new approach, so-called boundary variation diminishing (BVD), for reconstructions that minimize the discontinuities (jumps) at cell interfaces in Godunov type schemes. It is motivated by the observation that diminishing the jump at the cell boundary can effectively reduce the dissipation in numerical flux. Differently from the existing practices which seek high-order polynomials within mesh cells while assuming discontinuities being always at the cell interfaces, the BVD strategy presented in this paper switches between a high-order polynomial and a jump-like reconstruction that allows a discontinuity being partly represented within the mesh cell rather than at the interface. Excellent numerical results have been obtained for both scalar and Euler conservation laws with substantially improved solution quality in comparison with the existing methods. It is shown that new schemes of high fidelity for both continuous and discontinuous solutions can be devised by the BVD guideline with properly-chosen candidate reconstruction schemes. This work provides a simple and accurate alternative of great practical significance to the current high-order Godunov paradigm which overly pursues the smoothness within mesh cells under the questionable premiss that discontinuities only appear at cell interfaces.

1. Introduction

The high-resolution shock capturing schemes, which are now well-accepted as the main-stream numerical approach to solve hyperbolic conservation laws including the Euler equations for compressible gas dynamics, trace back to Godunov's scheme [13]. The original Godunov scheme is a conservative finite-volume method (FVM) with piece-wise constant reconstruction, and the fluxes at cell boundaries are computed by solving the exact Riemann problem given the piece-wise constant physical fields in the two neighboring cells which usually results in a jump at cell boundaries. In general, Godunov schemes consist of two essential steps in solution procedure, i.e. (I) reconstruct the physical fields to find the values at the left- and right- sides of cell boundaries, and (II) evaluate the numerical fluxes at cell boundaries that are needed in the FVM formulation to update the cell-integrated values for next time step.

For step (II), interested readers are referred to [38] for a monographic review. The main interest of this paper is limited to step (I), i.e. reconstruction. Continuous efforts have been devoted in the past half century to develop the original Godunov scheme into a class of high-resolution conservative schemes. Instead of the piece-wise constant approximation which leads to a first-order scheme, higher order polynomials have been used to improve the accuracy (convergence rate for smooth

* Corresponding author.
E-mail address: xiao.f.aa@m.titech.ac.jp (F. Xiao).

http://dx.doi.org/10.1016/j.jcp.2016.06.051
0021-9991/

solution). In order to get around the so-called Godunov barrier for linear schemes which states that any monotonic linear scheme can be of only first order, non-linear numerical dissipation has been introduced to high-order schemes to suppress spurious oscillations in the vicinity of discontinuities. The non-linear numerical dissipation has been devised in different forms seen in the literature as either flux limiters in flux-corrected transport (FCT) scheme [5,44] and total variation diminishing (TVD) scheme [14,36] or slope limiters in monotone upstream-centered schemes for conservation law (MUSCL) scheme [39,40]. The later gives a more straightforward interpretation of the polynomial-based reconstruction for high-order schemes, and shows a clear path to design high-resolution schemes using modified high-order polynomials. Representative schemes of this kind are piecewise parabolic method (PPM) method [9], essentially non-oscillatory scheme (ENO) [15,32,33,12] and weighted essentially non-oscillatory (WENO) scheme [21,19,31]. WENO concept provides a general framework to develop high-resolution schemes that are able to reach the highest possible accuracy over a given mesh stencil for smooth solution, and effectively stabilize the numerical solutions which include discontinuities. Successive works on WENO scheme are found in designing better smoothness indicators and nonlinear weights [16,4,3,30,17,20] to improve solution quality, as well as implementing the WENO concept to different discretization frameworks [10,25,28,22].

Starting from the piecewise constant approximation in the original Godunov scheme, the development of high-order shock capturing schemes has evidenced a history of efforts to reduce the difference between the reconstructed left- and right-side values at cell boundaries for smooth solutions. This observation, however to our knowledge, has not been paid enough attention, nor explored further as a prospective guideline to construct new schemes.

In this work, we propose a new guideline to design high-resolution schemes, called boundary variation diminishing (BVD) reconstruction. The BVD reconstruction shows consistent results with the observation gained for smooth solutions as mentioned above. More importantly, it also provides a principle to devise the reconstruction for discontinuity. We demonstrate in this paper the BVD reconstruction based on some existing schemes, i.e. the 5th-order WENO-Z method [4], the 5th-order targeted ENO (TENO5) method [12] and the THINC (Tangent of Hyperbola for INterface Capturing) method [42,43,34].

This paper is composed as follows. We present the BVD principle in Section 2, as well as the reconstruction schemes that fit separately smooth and discontinuous profiles as the building blocks for the BVD algorithm. The BVD-based numerical methods are then extensively verified in Section 3 with widely used benchmark tests, which demonstrate the significance and impact of the presented methods in resolving both smooth and discontinuous solutions. The paper ends with a brief summary in Section 4.

2. Numerical algorithm

We use a scalar conservation law in the following form to present the BVD algorithm

$$\frac{\partial u}{\partial t}+\frac{\partial f}{\partial x}=0, \tag{1}$$

where $u(x,t)$ is the solution function and $f(u)$ the flux function. For a hyperbolic equation, $\alpha=f'(u)$ is a real number, the characteristic speed.

We divide the computational domain into N non-overlapping cell elements, $I_i=[x_{i-\frac{1}{2}},x_{i+\frac{1}{2}}]$, $i=1,2,\cdots,N$. The mesh is assumed to be uniform across the computational domain for simplicity, $\Delta x=x_{i+\frac{1}{2}}-x_{i-\frac{1}{2}}$, which is not essential and formulations on non-uniform meshes can be constructed under the same concept.

Using an FVM framework, we define the volume-integrated average (VIA) of the solution function $u(x,t)$ for cell I_i as

$$\overline{u}_i(t)=\frac{1}{\Delta x}\int_{x_{i-\frac{1}{2}}}^{x_{i+\frac{1}{2}}}u(x,t)dx. \tag{2}$$

The VIA $\bar{u}_i$ of each cell $I_i=[x_{i-\frac{1}{2}},x_{i+\frac{1}{2}}]$ is updated by

$$\frac{d\bar{u}_i}{dt}=-\frac{1}{\Delta x}(\tilde{f}_{i+\frac{1}{2}}-\tilde{f}_{i-\frac{1}{2}}), \tag{3}$$

where the numerical fluxes at cell boundaries are computed by a Riemann solver

$$\tilde{f}_{i+\frac{1}{2}}=f^{\text{Riemann}}_{i+\frac{1}{2}}(u^L_{i+\frac{1}{2}},u^R_{i+\frac{1}{2}}), \tag{4}$$

using the left-side value u^L and right-side value u^R obtained from the reconstructions over left- and right-biased stencils. In spite of different variants, the Riemann flux is essentially upwinding and can be thus written in a canonical form as

$$f^{\text{Riemann}}_{i+\frac{1}{2}}(u^L_{i+\frac{1}{2}},u^R_{i+\frac{1}{2}})=\frac{1}{2}\left(f(u^L_{i+\frac{1}{2}})+f(u^R_{i+\frac{1}{2}})-|\tilde{\alpha}_{i+\frac{1}{2}}|(u^R_{i+\frac{1}{2}}-u^L_{i+\frac{1}{2}})\right), \tag{5}$$

where $\tilde{\alpha}_{i+\frac{1}{2}}$ stands for a characteristic speed in a hyperbolic equation. The last term in (5) can be interpreted as a numerical dissipation.

Our central task now is how to calculate the left-side value $u^L_{i+\frac{1}{2}}$ and right-side value $u^R_{i+\frac{1}{2}}$ for all cell boundaries $x_{i+\frac{1}{2}}$, $i = 1, 2, \cdots, N$.

2.1. Boundary variation diminishing (BVD) reconstruction

We propose a novel guideline for reconstruction that adaptively chooses proper interpolation functions so as to minimize the jump between the left- and right- side values, u^L and u^R, at cell interface. There might be different ways to realize this purpose, such as the method of least squares. For practical use, we elaborate on the simplest algorithm of the boundary variation diminishing (BVD) reconstruction for cell I_i used in this paper as follows.

i) Prepare two piece-wisely reconstructed interpolation functions, $\Phi_i^{<1>}(x)$ and $\Phi_i^{<2>}(x)$, of solution function $u(x)$ for each cell from the VIAs $\bar{u}_i$ available over the computational domain. The existing reconstruction methods, such as the (W)ENO and THINC described later, can be employed for this purpose. Without losing generality, we assume that $\Phi_i^{<1>}(x)$ is a higher-order polynomial-based interpolant, while $\Phi_i^{<2>}(x)$ might be of low-order but has better monotonicity (e.g. a sigmoid function is preferred for step-like discontinuity);

ii) Find $\Phi_i^{<p>}(x)$ and $\Phi_{i+1}^{<q>}(x)$ with p and q being either 1 or 2, so that the boundary variation (BV)

$$BV(\Phi)_{i+\frac{1}{2}} = |\Phi_i^{<p>}(x_{i+\frac{1}{2}}) - \Phi_{i+1}^{<q>}(x_{i+\frac{1}{2}})|, \tag{6}$$

is minimized;

iii) In case that a different choice for cell I_i is made when applying step ii) to the neighboring interface $x_{i-\frac{1}{2}}$, that is, $\Phi_i^{<q'>}(x)$ found to minimize

$$BV(\Phi)_{i-\frac{1}{2}} = |\Phi_{i-1}^{<p'>}(x_{i-\frac{1}{2}}) - \Phi_i^{<q'>}(x_{i-\frac{1}{2}})|, \tag{7}$$

with p' and q' being either 1 or 2, is different from $\Phi_i^{<p>}(x)$ found to minimize (6), we adopt the following criterion to uniquely determine the reconstruction function.

$$\Phi_i^{<p>}(x) = \begin{cases} \Phi_i^{<1>}(x), \text{ if } \left(\Phi_i^{<p>}(x_{i+\frac{1}{2}}) - \Phi_{i+1}^{<q>}(x_{i+\frac{1}{2}})\right)\left(\Phi_{i-1}^{<p'>}(x_{i-\frac{1}{2}}) - \Phi_i^{<q'>}(x_{i-\frac{1}{2}})\right) < 0, \\ \Phi_i^{<2>}(x), \text{ otherwise.} \end{cases} \tag{8}$$

iv) Compute the left-side value $u^L_{i+\frac{1}{2}}$ at $x_{i+\frac{1}{2}}$ and the right-side value $u^R_{i-\frac{1}{2}}$ at $x_{i-\frac{1}{2}}$ by

$$u^L_{i+\frac{1}{2}} = \Phi_i^{<p>}(x_{i+\frac{1}{2}}) \text{ and } u^R_{i-\frac{1}{2}} = \Phi_i^{<p>}(x_{i-\frac{1}{2}}). \tag{9}$$

Remark 1. The BVD algorithm reduces the reconstructed jumps at cell interfaces and thus the numerical dissipation term $ND_{i+\frac{1}{2}} = |\tilde{\alpha}|_{i+\frac{1}{2}}(u^R_{i+\frac{1}{2}} - u^L_{i+\frac{1}{2}})$ in Riemann solver (5), which can be expected to effectively improve the numerical solution.

Remark 2. For smooth solution, the BVD reconstruction naturally realizes the highest possible interpolation because interpolants of higher order tend to find an interface value closer to the continuous "true" solution.[1]

Remark 3. For discontinuous solution, pursuing higher order polynomials does not necessarily lead to the reduction of the reconstructed jumps at cell interfaces. It might imply the limitation of the current practice to use high-order polynomials for reconstructions.

Remark 4. By minimizing the jumps at cell boundaries, the BVD algorithm prefers a reconstruction that is able to represent a jump within the cell where a discontinuity exists. In this sense, the THINC reconstruction shown later is a better choice than a polynomial.

Remark 5. The BVD reconstruction provides a practical and effective guidance to construct high-fidelity schemes for resolving discontinuous solutions. As shown later, excellent numerical results can be obtained if the candidate reconstructions, $\Phi_i^{<1>}(x)$ and $\Phi_i^{<2>}(x)$, are properly chosen.

Remark 6. Another simpler alternative to (8) is

$$\Phi_i^{<p>}(x) = \begin{cases} \Phi_i^{<1>}(x), \text{ if } (\bar{u}_i - \bar{u}_{i+1})(\bar{u}_{i-1} - \bar{u}_i) < 0, \\ \Phi_i^{<2>}(x), \text{ otherwise.} \end{cases} \tag{10}$$

[1] Weierstrass approximation theorem guarantees the existence of such polynomials.

It does not make significant difference in our numerical experiments. It is also noted that adequate numerical results can be obtained without further adjustment after (8) or (10) in practice.

Remark 7. Other BV-equivalent quantities can be also used in the algorithm. For example, we have tested to minimize the total boundary variation (TBV), $TBV(\Phi)_i = |BV(\Phi)_{i-\frac{1}{2}}| + |BV(\Phi)_{i+\frac{1}{2}}|$ for cell i, which gives quite similar results but is more algorithmically complicated. Being aware of that the numerical dissipation appears eventually in a numerical scheme as $ND_{i+\frac{1}{2}} - ND_{i-\frac{1}{2}}$, we see another future option to minimize effective numerical dissipation (END), $END(\Phi)_i = |ND_{i+\frac{1}{2}} - ND_{i-\frac{1}{2}}|$, where $ND_{i+\frac{1}{2}} = |\tilde{\alpha}|_{i+\frac{1}{2}}(\Phi_{i+1}^{<p>}(x_{i+\frac{1}{2}}) - \Phi_i^{<p>}(x_{i+\frac{1}{2}}))$ is the numerical dissipation term.

2.2. The building-block reconstruction schemes

As shown in the BVD reconstruction algorithm, we need at least two building-block schemes to construct the candidate interpolation functions, $\Phi_i^{<1>}(x)$ and $\Phi_i^{<2>}(x)$. In order to enable the resulting scheme to accurately resolve both smooth and discontinuous solutions. We use two fifth-order (W)ENO reconstructions, known as the WENO-Z scheme [4] and the fifth-order targeted ENO (TENO5) scheme [12] to construct $\Phi_i^{<1>}(x)$, while use the THINC scheme [42,43] to construct $\Phi_i^{<2>}(x)$. We give a brief description for each of these algorithms as below.

2.2.1. The (W/T)ENO reconstructions for $\Phi_i^{<1>}(x)$

Both WENO-Z and TENO5 schemes compute the cell interface values by

$$\Phi_i^{<1>}(x_{i\pm\frac{1}{2}}) = \omega_0 u^{(0)}_{i\pm\frac{1}{2}} + \omega_1 u^{(1)}_{i\pm\frac{1}{2}} + \omega_2 u^{(2)}_{i\pm\frac{1}{2}}, \tag{11}$$

where $u^{(0)}$, $u^{(1)}$ and $u^{(2)}$ are computed from the third-order polynomials constructed separately over three slided 3-cell stencils.

$$\begin{aligned} u^{(0)}_{i-\frac{1}{2}} &= \frac{1}{3}\overline{u}_{i+2} - \frac{7}{6}\overline{u}_{i+1} + \frac{11}{6}\overline{u}_i,\ u^{(1)}_{i-\frac{1}{2}} = -\frac{1}{6}\overline{u}_{i+1} + \frac{5}{6}\overline{u}_i + \frac{1}{3}\overline{u}_{i-1},\ u^{(2)}_{i-\frac{1}{2}} = \frac{1}{3}\overline{u}_i + \frac{5}{6}\overline{u}_{i-1} - \frac{1}{6}\overline{u}_{i-2};\\ u^{(0)}_{i+\frac{1}{2}} &= \frac{1}{3}\overline{u}_{i-2} - \frac{7}{6}\overline{u}_{i-1} + \frac{11}{6}\overline{u}_i,\ u^{(1)}_{i+\frac{1}{2}} = -\frac{1}{6}\overline{u}_{i-1} + \frac{5}{6}\overline{u}_i + \frac{1}{3}\overline{u}_{i+1},\ u^{(2)}_{i+\frac{1}{2}} = \frac{1}{3}\overline{u}_i + \frac{5}{6}\overline{u}_{i+1} - \frac{1}{6}\overline{u}_{i+2}. \end{aligned} \tag{12}$$

It is noted that an uniform grid is assumed here for simplicity, but is not essential. The computation of the non-linear weights, $\omega_j,\ j = 0, 1, 2$, depends on the smoothness indicator which measures the smoothness of solution function $u(x)$. Different formulations are used in the WENO-Z and TENO5 reconstructions to compute the nonlinear weights. Interested readers are referred to [4] and [12] for details. We summarize the key formulations to calculate the non-linear weights in both WENO-Z and TENO5 schemes as follows.

For WENO-Z scheme, the non-linear weights are computed by

$$\omega_k = \frac{\alpha_k}{\sum_{k=0}^{2}\alpha_k},\ \alpha_k = d_k\left(1 + \left(\frac{\tau_5}{\beta_k + \epsilon}\right)^q\right),\ \tau_5 = |\beta_2 - \beta_0|,\ k = 0, 1, 2, \tag{13}$$

where d_k is the optimal weight to recover the full 5th-order scheme with the values $d_0 = 0.1,\ d_1 = 0.6$ and $d_2 = 0.3$. $q = 1$ is recommended to control the excessive numerical dissipation in non-smooth region. The smoothness indicator β_k is defined following [19] by

$$\beta_j = \sum_{l=1}^{2}\int_{x_{i-\frac{1}{2}}}^{x_{i+\frac{1}{2}}} \Delta x^{2l-1}\left(\frac{d^l u^{(j)}(x)}{dx^l}\right)^2 dx, \quad j = 0, 1, 2. \tag{14}$$

For the TENO5 scheme, the smoothness measure is defined as

$$\gamma_k = \left(C + \frac{\tau_k}{\beta_k + \epsilon}\right)^q,\ k = 0, \ldots, K-3, \tag{15}$$

where $K = 5$ is the maximum order for the TENO5 scheme. $C = 1$ and $q = 6$ are suggested in [12] to balance between numerical dissipation and computation robustness. The core of the TENO scheme is the ENO-like stencil selection procedure. Firstly, the normalization of the smoothness measure is given by

$$\chi_k = \frac{\gamma_k}{\sum_{k=0}^{2}\gamma_k},\ k = 0, 1, 2, \tag{16}$$

then the cut-off function is defined from χ_k as

$$\delta_k = \begin{cases} 0, & \text{if } \chi_k < C_T \\ 1, & \text{otherwise} \end{cases} \quad k = 0, 1, 2, \tag{17}$$

where C_T is set to 10^{-5}. Finally, the nonlinear weight can be obtained from a renormalization procedure as

$$\omega_k = \frac{d_k \delta k}{\sum_{k=0}^{2} d_k \delta_k}, \quad k = 0, 1, 2. \tag{18}$$

As discussed in [12], the TENO5 scheme is superior to the WENO-Z scheme in resolving discontinuities with less numerical dissipation. We compared the two schemes in some numerical tests and observed that both work well under the BVD framework, and the original properties of WENO-Z and TENO5 can be observed when implemented with the BVD principle.

2.2.2. The THINC reconstruction for $\Phi_i^{<2>}(x)$

Being a sigmoid function, hyperbolic tangent function is a differentiable and monotone function that fits well a step-like discontinuity. A class of VOF (volume of fluid) schemes, so-called THINC (Tangent of Hyperbola for INterface Capturing), has been devised to compute moving interfaces in multiphase flow simulations [42,43,34,7] based on the hyperbolic tangent function. In the present work, we use THINC reconstruction as the second candidate interpolation function $\Phi_i^{<2>}(x)$ in the BVD algorithm,

$$\Phi_i^{<2>}(x) = u_{min} + \frac{u_{max}}{2}\left(1 + \gamma \tanh\left(\beta\left(\frac{x - x_{i-\frac{1}{2}}}{x_{i+\frac{1}{2}} - x_{i-\frac{1}{2}}} - \tilde{x}_i\right)\right)\right), \tag{19}$$

where $u_{min} = \min(\bar{u}_{i-1}, \bar{u}_{i+1})$, $u_{max} = \max(\bar{u}_{i-1}, \bar{u}_{i+1}) - u_{min}$ and $\gamma = \mathrm{sgn}(\bar{u}_{i+1} - \bar{u}_{i-1})$. Parameter β is used to control the jump thickness. We use a constant value of $\beta = 1.6$ for all numerical tests in this paper. The unknown $\tilde{x}_i$, which represents the location of the jump center, is computed from the constraint condition, $\bar{u}_i = \frac{1}{\Delta x}\int_{x_{i-\frac{1}{2}}}^{x_{i+\frac{1}{2}}} \Phi_i^{<2>}(x)dx$.

Rather than showing explicitly the formula to calculate $\tilde{x}_i$, we give the expressions for the reconstructed left- and right-end values of cell I_i by

$$\begin{aligned} \Phi_i^{<2>}(x_{i+\frac{1}{2}}) &= u_{min} + \frac{u_{max}}{2}\left(1 + \gamma \frac{\tanh(\beta) + A}{1 + A\tanh(\beta)}\right), \\ \Phi_i^{<2>}(x_{i-\frac{1}{2}}) &= u_{min} + \frac{u_{max}}{2}(1 + \gamma A), \end{aligned} \tag{20}$$

where $A = \frac{B/\cosh(\beta) - 1}{\tanh(\beta)}$, $B = \exp\left(\gamma\beta\left(2\frac{\bar{u}_i - \bar{u}_{min} + \epsilon}{u_{max} + \epsilon} - 1\right)\right)$ and $\epsilon = 10^{-20}$.

Remark 8. We also experimented using piece-wise constant and MUSCL reconstructions for $\Phi_i^{<2>}(x)$, and find that the BVD algorithm results in a less oscillatory solution without noticeable increase in numerical dissipation in comparison with the computations which only use WENO-Z or TENO5 reconstructions. Another combination that uses MUSCL for $\Phi_i^{<1>}(x)$ and THINC for $\Phi_i^{<2>}(x)$ gives significant improvement in resolving contact discontinuities in numerical solutions as well.

We refer to the BVD algorithm using WENO-Z and THINC reconstructions as BVD-WENOZ-THINC method, and the BVD algorithm using TENO5 and THINC reconstructions as BVD-TENO5-THINC method in this paper. More explicitly, WENO-Z reconstruction is used for $\Phi_i^{<1>}(x)$ and THINC for $\Phi_i^{<2>}(x)$ in BVD-WENOZ-THINC method, while TENO5 reconstruction is used for $\Phi_i^{<1>}(x)$ and THINC reconstruction for $\Phi_i^{<2>}(x)$ in BVD-TENO5-THINC method.

For Euler equations, the (W/T)ENO and THINC reconstructions are implemented to the characteristic variables, and the minimization in the BVD algorithm is conducted in terms of the primitive variables separately, i.e. density, velocity and pressure. We also experimented to apply the BVD algorithm in terms of the characteristic variables, and include the corresponding results in numerical tests of two interacting blast waves (1D) and double Mach reflection (2D). It is observed that minimizing the primitive variables in the BVD algorithm leads to slightly less dissipated numerical solutions even though the difference is not much significant.

We use Roe's Riemann solver [29] to calculate the numerical fluxes. The five stage fourth order SSP Runge–Kutta method [35] is used for time marching with a CFL number of 0.4 in the numerical tests presented next.

The multi-dimensional reconstruction in this work is carried out in a dimension-by-dimension fashion [6,37]. Rather than high-order Gaussian integration, the numerical fluxes on the cell interfaces are evaluated by the mid-point rule for simplicity as commonly used in finite volume method.

3. Numerical results

In this section, the numerical results of some benchmark tests for scalar and Euler conservation laws are presented to illustrate the performance of the BVD-based methods described above.

Table 1
Numerical errors and convergence rates for 1D advection equation, $t = 2.0$.

N	BVD-WENOZ-THINC scheme				WENO-Z scheme			
	L_1 error	Order	L_∞	Order	L_1 error	Order	L_∞	Order
20	2.14e−04		3.65e−06		2.14e−04		3.65e−06	
40	6.40e−06	5.07	1.03e−05	5.10	6.40e−06	5.07	1.03e−05	5.10
80	2.00e−07	5.00	3.18e−07	5.02	2.00e−07	5.00	3.18e−07	5.02
160	6.32e−09	4.99	9.96e−09	5.00	6.32e−09	4.99	9.96e−09	5.00
320	2.04e−10	4.00	3.20e−10	4.96	2.04e−10	4.00	3.20e−10	4.96

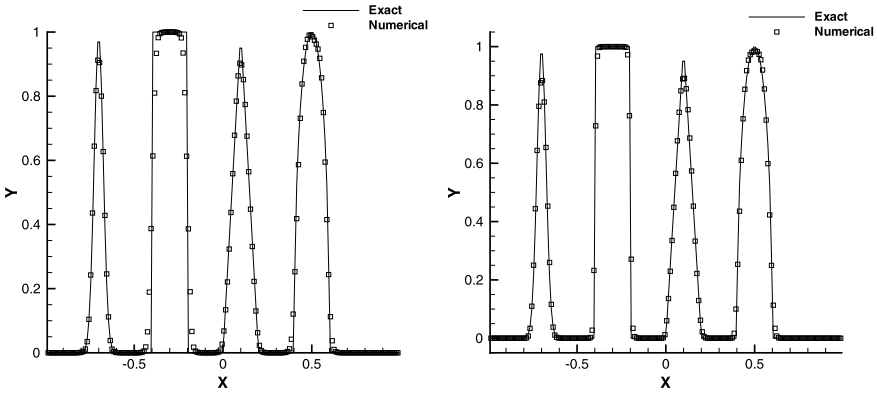

Fig. 1. Numerical result of Jiang and Shu's test after one period ($t = 2.0$) with 200 grid cells computed by WENO-Z scheme (left) and BVD-WENOZ-THINC scheme (right).

3.1. Scalar conservation laws

3.1.1. Linear advection equation

Firstly, we consider the following 1D linear advection equation

$$u_t + u_x = 0. \tag{21}$$

Accuracy test for 1D advection equation. An initially smooth profile defined by $u(x, 0) = \sin(\pi x),\ x \in [-1, 1]$ is advected. The L_1 and L_∞ errors of VIA after one period are measured under different grid resolutions. Shown in Table 1, the numerical errors of BVD-WENOZ-THINC are identical to that of WENO-Z for all grid resolutions. It proves that the BVD algorithm perfectly retrieves the 5th-order WENO scheme for smooth solution.

Jiang and Shu's test. The initial condition of this test includes both discontinuities and smooth profiles. We set the initial condition as

$$u(x,0) = \begin{cases} \frac{1}{6}\left(G(x,\beta,z-\delta) + G(x,\beta,z+\delta) + 4G(x,\beta,z)\right), & -0.8 \leqslant x \leqslant -0.6, \\ 1, & -0.4 \leqslant x \leqslant -0.2, \\ 1 - |10(x-0.1)|, & 0.0 \leqslant x \leqslant 0.2, \\ \frac{1}{6}\left(F(x,\alpha,a-\delta) + F(x,\alpha,a+\delta) + 4F(x,\alpha,a)\right), & 0.4 \leqslant x \leqslant 0.6, \\ 0, & \text{otherwise}, \end{cases} \tag{22}$$

where the computation domain is $[-1, 1]$. The function F and G is defined by

$$G(x,\beta,z) = \exp\left(-\beta(x-z)^2\right),\ F(x,\alpha,a) = \sqrt{\max(1-\alpha^2(x-a)^2, 0)}, \tag{23}$$

and the coefficients to determine the initial profile are given by

$$a = 0.5,\ z = 0.7,\ \delta = 0.005,\ \alpha = 10.0,\ \beta = \log 2/(36\delta^2). \tag{24}$$

The numerical results are shown in Fig. 1. Compared to the WENO-Z method (Fig. 1 (left)), the BVD-WENOZ-THINC method (Fig. 1 (right)) can resolve the sharp discontinuity with significantly improved quality while keeping the smooth profile with good resolution.

Advection of jump discontinuity. In this test, we analyze the sharpness of a single discontinuity for advection equation. Initially, the discontinuity is located at $x = 0.5$, defined as

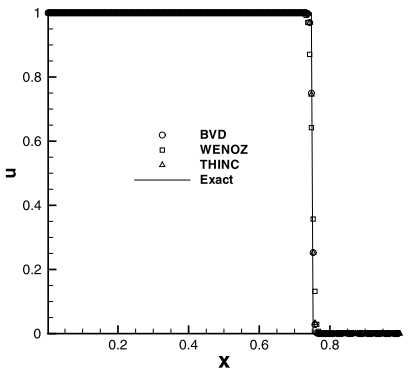

Fig. 2. The advection of jump discontinuity computed by WENO-Z, THINC, and BVD-WENOZ-THINC scheme at $t = 0.25$.

Table 2
Comparison of discontinuity thickness for the advection of jump discontinuity.

	WENOZ	THINC	BVD-WENZ-THINC
$\delta_{thickness}$	3.51015	2.02722	2.01354

Table 3
Numerical errors and convergence rates for 1D Burgers equation at $t = 1/(2\pi)$.

N	L_1 error	Order of accuracy	L_∞ error	Order of accuracy
20	3.00e−04		2.07e−03	
40	1.66e−05	4.18	2.15e−04	3.27
80	7.36e−07	4.49	9.94e−06	4.43
160	2.65e−08	4.79	3.56e−07	4.80

$$u(x,0) = \begin{cases} 1, & 0.0 \leqslant x \leqslant 0.5 \\ 0, & \text{otherwise.} \end{cases} \tag{25}$$

To examine how the BVD algorithm improves resolving discontinuities, we display the numerical results at $t = 0.25$ on a 200-cell mesh computed by WENO-Z, THINC and BVD-WENOZ-THINC scheme respectively in Fig. 2. It can be observed that steeper jumps are obtained by both THINC and BVD-WENOZ-THINC schemes than WENO-Z scheme. For further quantitative evaluation, we introduce the thickness measurement of a discontinuity proposed in [24] as

$$\delta_{thickness} = \frac{\alpha_{jump}}{\Delta x} \frac{1}{\max(\frac{\delta u}{\delta x})} = \frac{\alpha_{jump}}{\max(u_j - u_{j-1})} \tag{26}$$

where $\alpha_{jump} = 1$ for this test. The results are shown in Table 2. As expected, the thickness of discontinuity for WENO-Z scheme is much larger than that of the BVD-WENOZ-THINC and THINC schemes. Although the difference of thickness between BVD-WENOZ-THINC and THINC scheme is small, the BVD-WENOZ-THINC scheme looks even better than the pure THINC computation in resolving a discontinuity, which manifests the effectiveness of the BVD based schemes in minimizing numerical dissipation.

3.1.2. Inviscid Burgers equation

We consider the 1D inviscid Burger's equation

$$u_t + \left(\frac{u^2}{2}\right)_x = 0. \tag{27}$$

Here we will give two examples for inviscid Burgers equation.

Burgers equation with an initial sine wave. In this test, a sine wave is given as the initial profile, which will develop into a shock wave after $t = 1.5/\pi$ due to the convexity of the Burgers flux. Firstly, in order to measure the convergence rate of the BVD-based algorithm, we carried out the computation with BVD-WENOZ-THINC method up to $t = 0.5/\pi$. The numerical errors are shown in Table 3, which demonstrate nearly a 5th-order accuracy. We also show the numerical results computed on a 100-cell mesh at $t = 1.5/\pi$ in Fig. 3 (left). We can see that the shock wave in this test can be resolved within only two mesh cells.

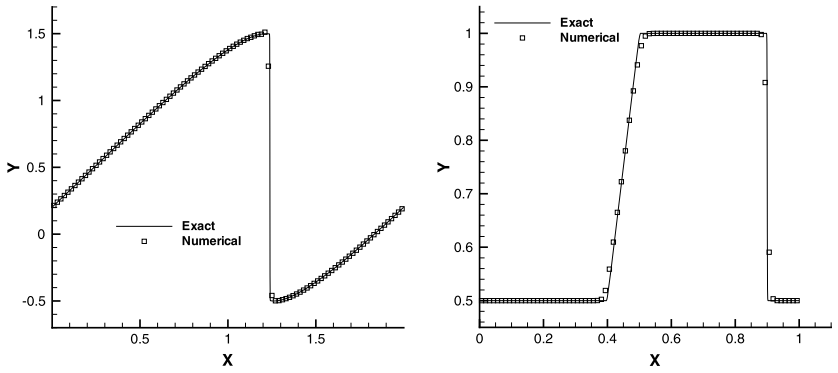

Fig. 3. Numerical results of Burgers equation computed by BVD-WENOZ-THINC scheme. Left: Solution at $t = 1.5/\pi$ on a 100-cell mesh with a sine-wave initial condition. Right: Solution at $t = 0.2$ on a 80-cell mesh with a square pulse initial condition (28).

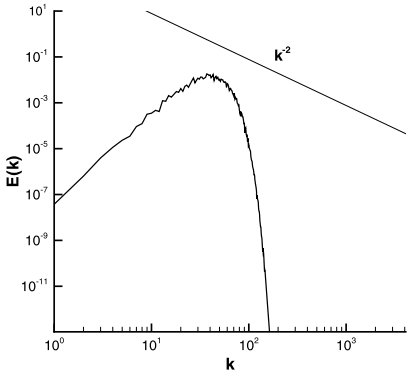

Fig. 4. The prescribed energy spectrum at $t = 0$.

Burgers equation with shock and rarefaction waves. The initial condition of this benchmark test is given by

$$u(x,0) = \begin{cases} 1, & 0.3 \leqslant x \leqslant 0.75, \\ 0.5, & \text{otherwise}. \end{cases} \tag{28}$$

Both shock and rarefaction wave are included in this test. The numerical results at $t = 0.2$ are shown in Fig. 3 (right). The BVD-WENOZ-THINC scheme can reproduce both the shock and expansion fan with good accuracy.

3.1.3. Burgers turbulence

A well-known observation is that Godunov type methods using Riemann solvers, even of high order, generates excessive numerical dissipation to high wave number range, and might not be properly used in large eddy simulations for turbulent flows of high Reynolds number. In order to examine the numerical dissipation of the proposed methods in simulating turbulent flows, we solved Burger turbulence problem introduced in [2]. Burgers equation with viscosity is written as

$$u_t + \left(\frac{u^2}{2}\right)_x = \nu u_{xx}, \tag{29}$$

where $\nu = 1 \times 10^{-4}$ is the viscosity coefficient.

The computational domain is $[0, 1]$ with periodical boundary conditions. The Fourier representation of the velocity function is $u(x,t) = \sum_q \hat{u}_q(t) exp(ik_q x)$. The energy of single mode k_q is calculated by $E(k_q, t) = u(k_q, t)^2$. The initial condition is prescribed in terms of energy spectrum same as in [2], i.e.

$$E(k,0) = A\sigma k^4 exp(-0.5\sigma^2 k^2), \tag{30}$$

where constant $A = \frac{U_0^2}{3\sqrt{2\pi}}$ with $U_0^2 = \langle u_0(x)^2 \rangle$ the mean kinetic energy at $t = 0$ and $\sigma = 0.05/2\pi$. The initial velocity field is given through the means of Wiener process.

Shown in Fig. 4, the initial kinetic energy is concentrated to the low wave numbers, which is then transfered to the high wave number range. In the present paper, the numerical results from WENO-Z scheme on a fine mesh (8192 cells) are referred to as the DNS (Direct numerical simulation) solutions. We computed the Burgers turbulence for a truncated

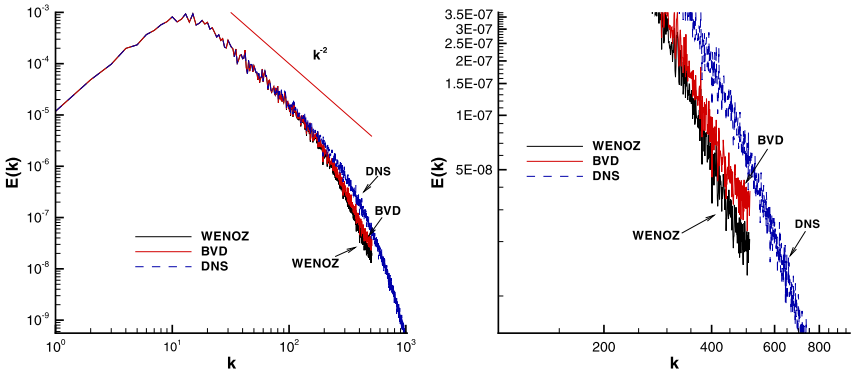

Fig. 5. The energy spectra of Burgers turbulence at $t = 0.06$ on 1024 cells computed by WENO-Z and BVD-WENOZ-THINC schemes. The DNS results are computed on 8192 cells by WENO-Z scheme. Displayed are the spectra for the whole region (left) and the zoomed-in view of high-wave number region (right).

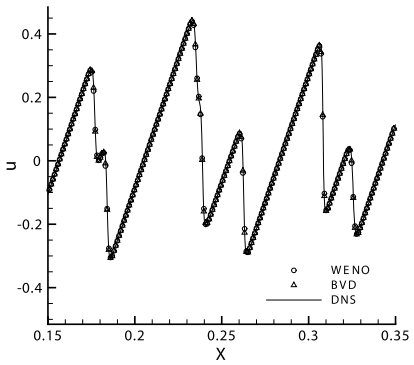

Fig. 6. Velocity distribution at $t = 0.06$ computed by WENO-Z and BVD-WENOZ-THINC schemes. The DNS results are calculated by WENO-Z scheme on 8192 cells.

spectral range on a mesh of 1024 cells by both WENO-Z and BVD-WENOZ-THINC methods. The energy spectrum at $t = 0.06$ are plotted in Fig. 5. It is found that the BVD-WENOZ-THINC method effectively reduces the numerical dissipation in high wave number range compared to the WENO-Z scheme. Also, the velocity distribution in physical field from $x = 0.15$ to $x = 0.35$ is given in Fig. 6. It shows that BVD-WENZ-THINC scheme can achieve better resolution for velocity field than WENOZ scheme. Consistent to the results in all other numerical tests, significant improvement in numerical dissipation can be obtained by the BVD algorithm, which is thus expected to be a general and practical remedy to existing methods that are too numerically dissipative to simulate turbulence flows of high Reynolds numbers.

3.1.4. Buckley Leverett equation

1D Buckley Leverett equation reads

$$u_t + \left(\frac{4u^2}{4u^2 + (1-u)^2} \right)_x = 0. \tag{31}$$

Square pulse problem. The initial condition is set to be a square pulse,

$$u(x,0) = \begin{cases} 1, & -\dfrac{1}{2} \leqslant x \leqslant 0, \\ 0, & \text{otherwise}. \end{cases} \tag{32}$$

The solution to this test is a mixture containing shock, rarefaction and contact discontinuity. We carried out the computation up to $t = 0.4$. The numerical result of BVD-WENOZ-THINC method is given in Fig. 7. We can see that the result is of good quality even with such a low resolution grid.

3.2. 1D Euler equations

In this subsection, we present the numerical results of some benchmark shock-tube tests for 1D Euler equations to verify our new schemes for resolving the shock wave, contact discontinuity and rarefaction wave in compressible gas flows.

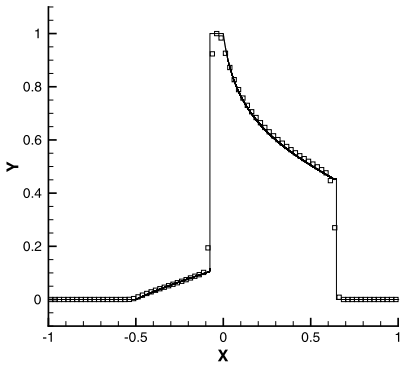

Fig. 7. Numerical solution of Buckley Leverett problem at $t = 0.2$ with 80 cells.

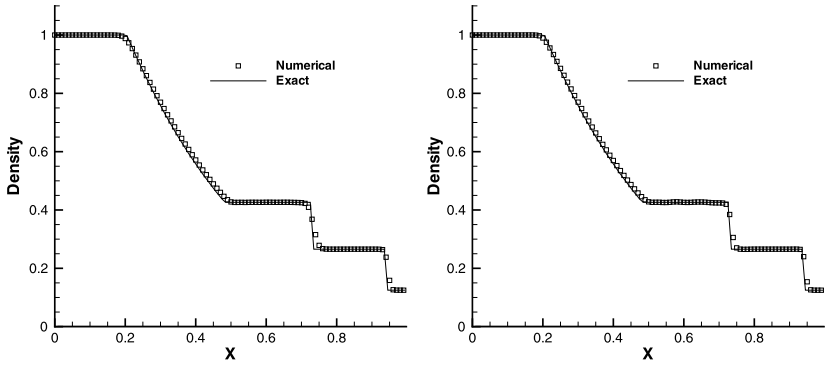

Fig. 8. Sod's problem at $t = 0.25$ with 100 cells solved by WENO-Z method (left) and BVD-WENOZ-THINC method (right).

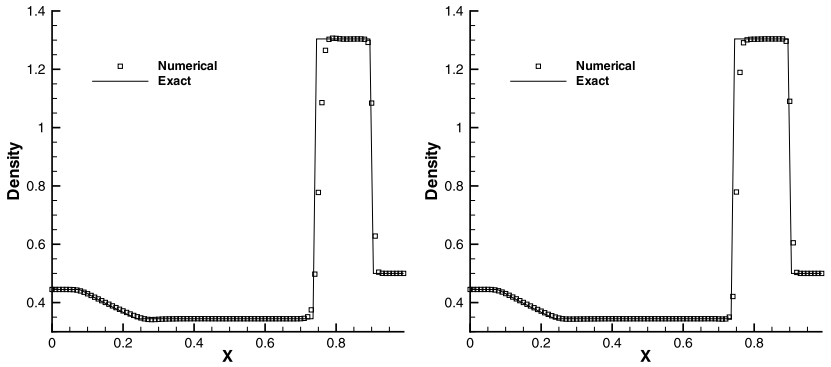

Fig. 9. Same as Fig. 8, but for Lax problem at $t = 0.16$.

Sod's problem. The initial condition is given by

$$(\rho_0, v_0, p_0) = \begin{cases} (1, 0, 1), & 0 \leqslant x \leqslant 0.5, \\ (0.125, 0, 0.1), & \text{otherwise}. \end{cases} \tag{33}$$

The mesh number is 100 in this test. The results from both WENO-Z and BVD-WENOZ-THINC are presented in Fig. 8 for comparison. It is observed that BVD-WENOZ-THINC scheme resolves better the contact discontinuity and the expansion front, while the solution of WENO-Z looks more dissipative.

Lax's problem. This is another widely used benchmark test with the initial condition given by

$$(\rho_0, v_0, p_0) = \begin{cases} (0.445, 0.698, 3.528), & 0 \leqslant x \leqslant 0.5, \\ (0.5, 0, 0.571), & \text{otherwise}. \end{cases} \tag{34}$$

We show the numerical results at $t = 0.16$ for both WENO-Z and BVD-WENOZ-THINC in Fig. 9 for comparison. It can be seen again that our scheme can reproduce sharp contact discontinuity and shock wave, while maintaining the high accuracy for

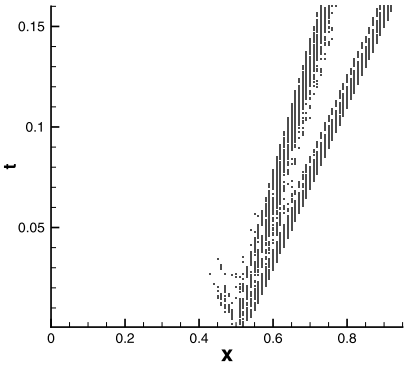

Fig. 10. The mesh cells where the THINC reconstruction for density is implemented based on the BVD principle corresponding to Lax problem in Fig. 9.

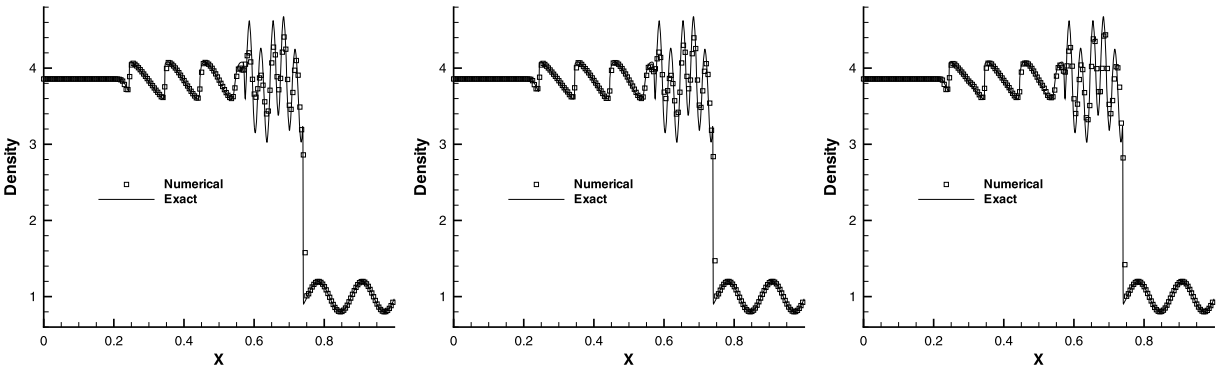

Fig. 11. Numerical results of shock–turbulence interaction at $t = 0.18$ with 200 cells. Displayed are solutions of density computed by WENO-Z (left), BVD-WENOZ-THINC (middle) and BVD-TENO5-THINC (right).

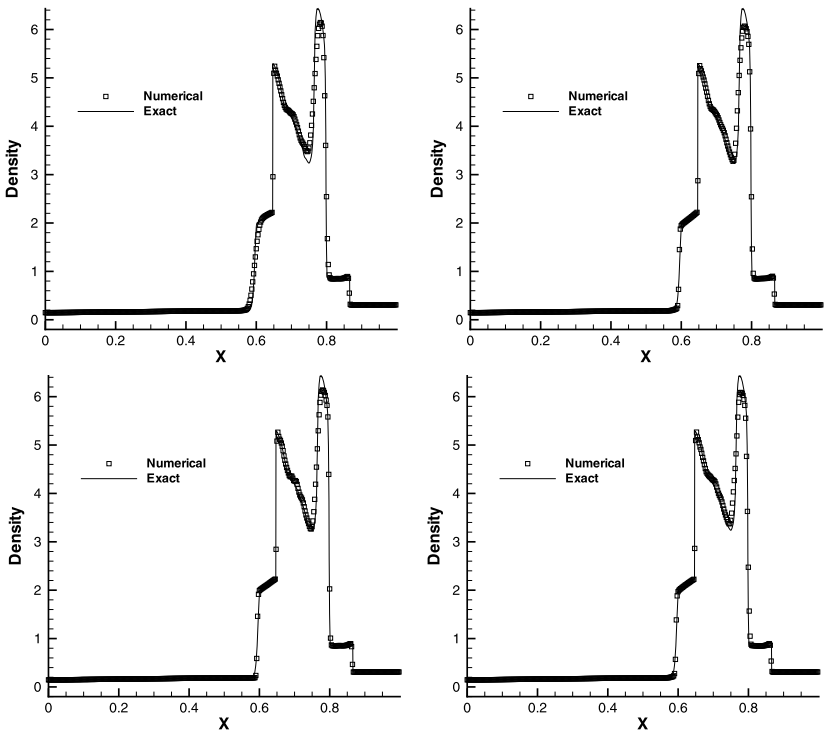

Fig. 12. Numerical results of two interacting blast waves at $t = 0.038$ with 400 cells. Displayed are solutions of density computed by WENO-Z (top left), BVD-WENOZ-THINC (top right), BVD-TENO5-THINC (bottom left) and BVD-WENOZ-THINC-C (bottom right).

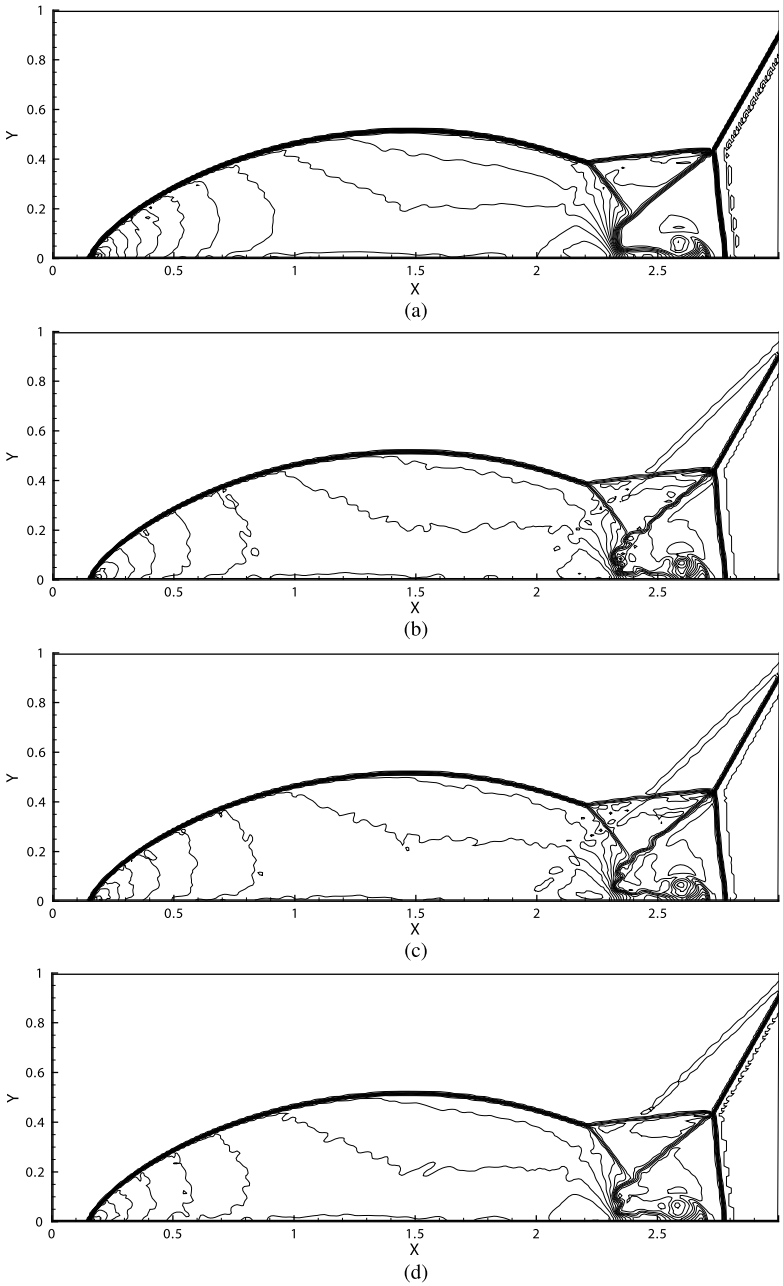

Fig. 13. Numerical results of double Mach reflection at $t = 0.2$ with 100×320 cells by WENO-Z (a), BVD-WENOZ-THINC (b), BVD-TENO5-THINC (c) and BVD-WENOZ-THINC-C (d).

smooth profile. We plot the t–x diagram in Fig. 10 to demonstrate the cells where the THINC reconstruction is implemented. It reveals that the discontinuities, both contact discontinuity and shock, are properly identified by the BVD criterion. It is noteworthy that the BVD algorithm automatically chooses the reconstructions that minimize the BV values rather than explicitly identifies the "troubled" cells using the ad hoc total variation bounded (TVB) indicator [8].

Shock–turbulence interaction. The initial condition of this test is specified by

$$(\rho_0, v_0, p_0) = \begin{cases} (3.857143, 2.629369, 10.333333), & \text{when } x < 0.1, \\ (1.0 + 0.2\sin(50x - 25), 0, 1.0), & \text{when } x \geqslant 0.1. \end{cases} \tag{35}$$

The computational domain is $[0, 1]$ and we perform the calculation up to $t = 0.18$ on a mesh of 200 cells. The numerical results of WENO-Z, BVD-WENOZ-THINC and BVD-TENO5-THINC are shown in Fig. 11. It is observed that the BVD algorithm

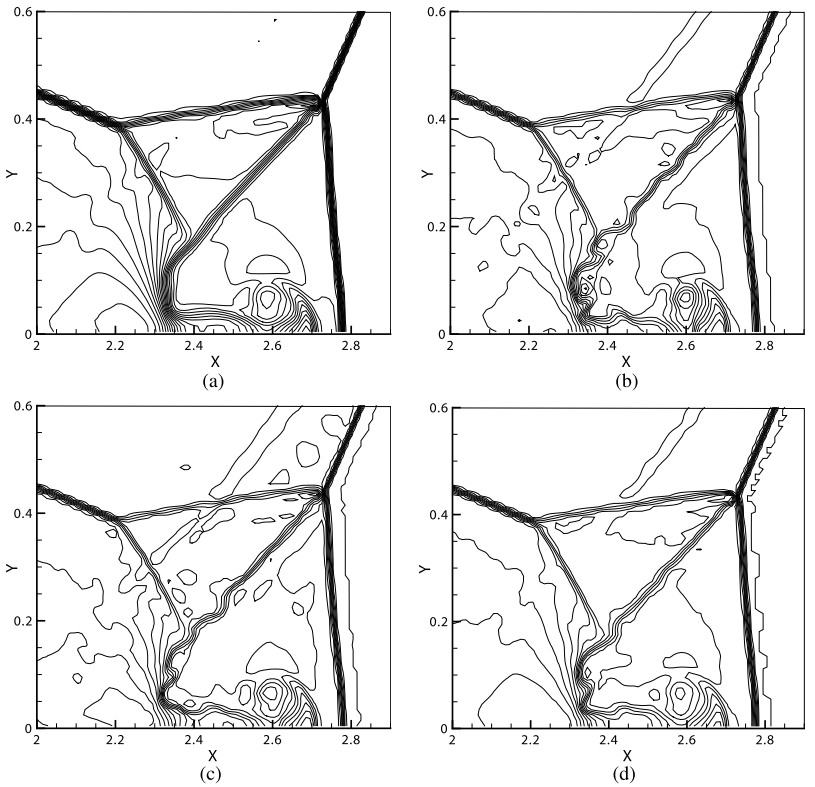

Fig. 14. The Zoomed-in parts of numerical results shown in Fig. 13. (a): WENO-Z, (b): BVD-WENOZ-THINC, (c): BVD-TENO5-THINC, (d): BVD-WENOZ-THINC-C.

does not make significant difference to the smooth solution where the polynomial-based reconstructions are preferred as in the linear advection tests. The difference between WENO-Z and TENO5 is clearly seen in the results.

Two interacting blast waves. This is a 1D benchmark test including more complicated interactions and discontinuous structures. Initially we set the following condition for state variables,

$$(\rho_0, v_0, p_0) = \begin{cases} (1, 0, 1000), & 0 \leqslant x \leqslant 0.1, \\ (1, 0, 0.01), & 0.1 < x < 0.9, \\ (1, 0, 100), & \text{otherwise}. \end{cases} \tag{36}$$

The reflection boundary is set to the left and right ends of computational domain. This test includes the multiple interaction of strong shock waves, density discontinuities and rarefaction waves. The numerical solutions of density computed by WENO-Z, BVD-WENOZ-THINC and BVD-TENO5-THINC are given in Fig. 12. The common headache to nearly all existing shock-capturing schemes is the overly smeared density discontinuities in the numerical solutions, as can be seen in the result of WENO-Z in Fig. 12 (top-left). The numerical results of BVD-WENOZ-THINC (Fig. 12 (top-right)) and BVD-TENO5-THINC (Fig. 12 (bottom-left)) are among the best ones ever reported in the literature to this benchmark test. Especially, the resolution of the left-most density discontinuity is resolved within less than four cells, which is much superior to any other existing shock capturing schemes without artificial compression steepening treatment. We also implemented the BVD algorithm to minimize the boundary variations of characteristic variables as another practical alternative. The results of such an implementation of the BVD-WENOZ-THINC scheme, referred to as BVD-WENOZ-THINC-C, is plotted in Fig. 12 (bottom-right). Minimizing the boundary variations of the characteristic variables results in a slightly dissipated solution in comparison with the primitive variables in the BVD algorithm although the difference is not much significant.

3.3. 2D Euler equations

Implementing the BVD algorithm in multiple dimensions on structured grids is straightforward. In order to verify the proposed methods in multi-dimensions, we solved two benchmark tests suggested in [41] for 2D Euler equations.

Double Mach reflection. This benchmark test contains both shock wave and contact discontinuity, and is usually used to verify numerical schemes in capturing strong shocks and vortical structures, which requires a numerical scheme to be optimized in terms of suppressing both numerical oscillation and dissipation.

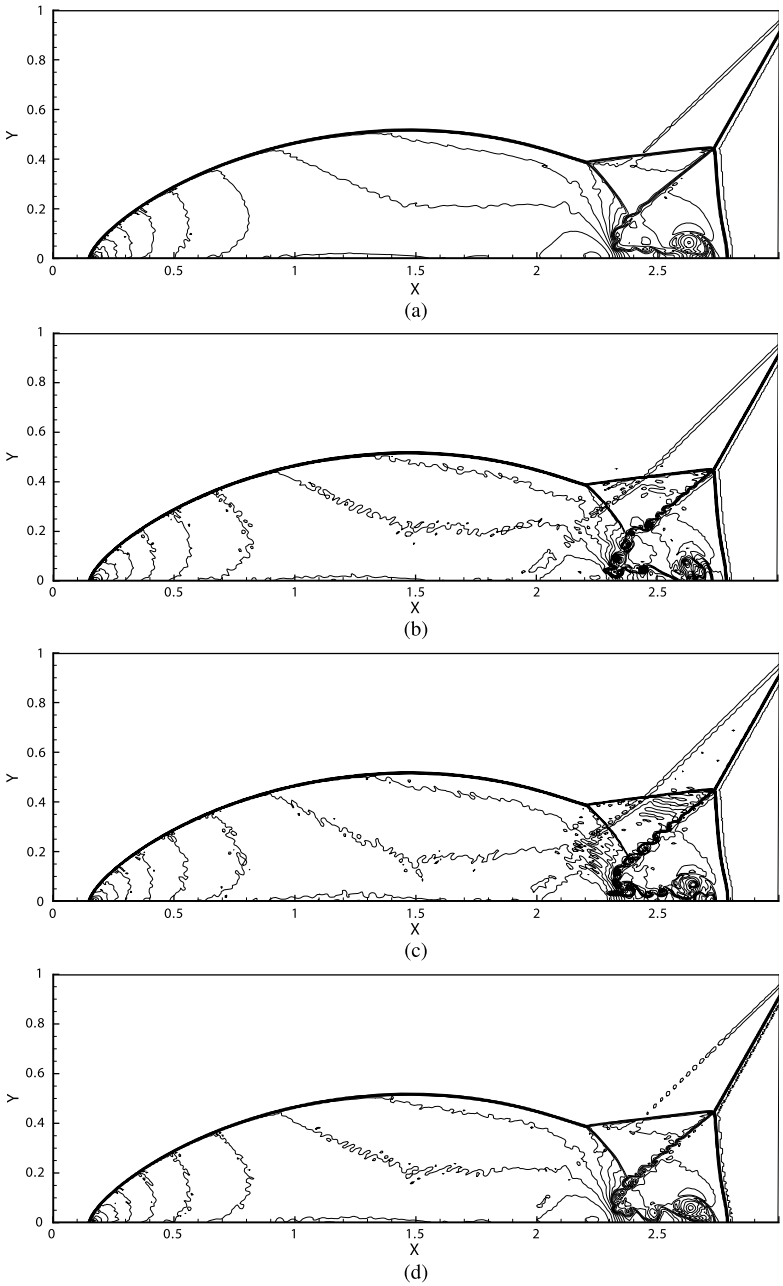

Fig. 15. Same as Fig. 13, but on a 200×620 mesh.

We computed the solution up to $t = 0.2$ on two meshes of different resolutions. The numerical results of WENO-Z, BVD-WENOZ-THINC, BVD-TENO5-THINC and BVD-WENOZ-THINC-C on a 100×320 mesh are shown in Fig. 13 with the zoomed-in part in Fig. 14. The results on a 200×640 mesh are displayed in Fig. 15 with the zoomed-in region in Fig. 16. The vortex structures resulted from Kelvin–Helmholtz instabilities along the slip line are the key features to evaluate the intrinsic numerical dissipation of the tested schemes. On the coarse mesh of 100×320 cells, the WENO-Z is not able to produce the vortex structures along the slip line, while all BVD-based methods resolved adequately the vortex structures. The numerical result of BVD-WENOZ-THINC-C looks slightly more dissipative compared to BVD-WENOZ-THINC, but still shows the effectiveness of the BVD algorithm in preserving the vortex solutions.

On the 200×640 mesh, the numerical solutions from all BVD-based methods are of good quality comparable to those obtained using discontinuous Galerkin (DG) method with even more degrees of freedom (DOFs) [26,27,23,11].

Mach 3 step tunnel. In this benchmark test, a right-moving Mach 3 flow in a tunnel with a forward step and reflective boundaries generates complex flows due to the interactions among shocks, density disturbances and shear flows.

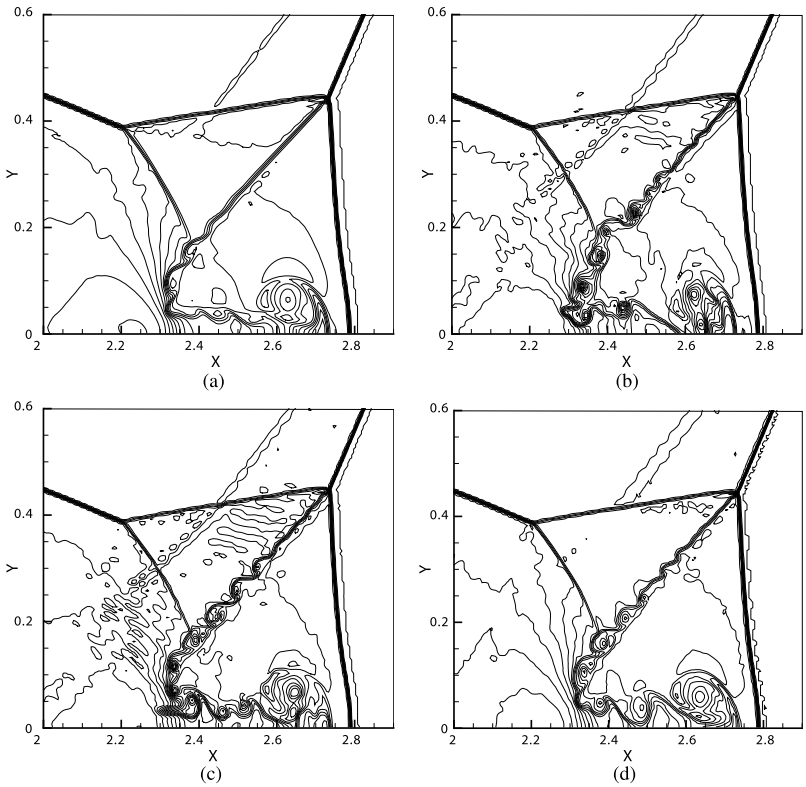

Fig. 16. Same as Fig. 14, but on a 200×640 mesh.

We show the numerical results of WENO-Z, BVD-WENOZ-THINC and BVD-TENO5-THINC at $t = 4.0$ on a 100×300 mesh in Fig. 17. All shock waves are well resolved by three schemes without significant difference, while the vortex structures starting from the front triple point look different. The vortex structures are more clearly resolved by both BVD-WENOZ-THINC and BVD-TENO5-THINC methods. It is noted again that the BVD-WENOZ-THINC and BVD-TENO5-THINC methods produce the competitive numerical results for the vortex structures on a relatively lower mesh resolution in comparison with other existing methods.

4. Summary

We have proposed a new guideline to construct high-resolution Godunov type schemes to resolve both smooth and discontinuous solutions. The basic idea, so-called BVD (boundary variation diminishing), is to reconstruct the solution functions so that the jumps at cell boundaries are minimized, which effectively reduces the numerical dissipation in the resulting schemes. The BVD reconstruction automatically realizes the highest possible polynomial interpolation for smooth profile, whilst prefers other forms of reconstructions in the presence of discontinuities. As a result, the BVD reconstruction mitigates the questionable premiss that discontinuities only appear at cell interfaces in the current paradigm of high-order Godunov schemes.

We have implemented the BVD algorithm with the existing schemes, i.e. WENO-Z, TENO5 and THINC schemes, as the building blocks. The BVD algorithm provides a reliable switching mechanism to reconstruct the solution function for both smooth profile and discontinuity. Excellent numerical results have been obtained for both scalar the Euler conservation laws, which show a substantial improvement in comparison with the existing methods including the high-order and less-dissipative methods.

Differently from the TVB troubled-cell indicator [8] that depends on ad hoc parameters, the BVD algorithm automatically chooses the reconstructions that minimize the BV values. Our preliminary analysis of the BVD algorithm under the nodal type discontinuous Galerkin (DG) (or more generally the flux reconstruction (FR) [18]) framework with the WENO limiting projection shows that BVD provides a more reliable switching compared to the prevailing TVB troubled-cell indicator [1].

Not limited to the (W/T)ENO and THINC schemes used in the present work, the BVD concept as a general platform of more profound impact can be used with other candidate reconstructions to further explore high-fidelity schemes for capturing both smooth and discontinuous solutions.

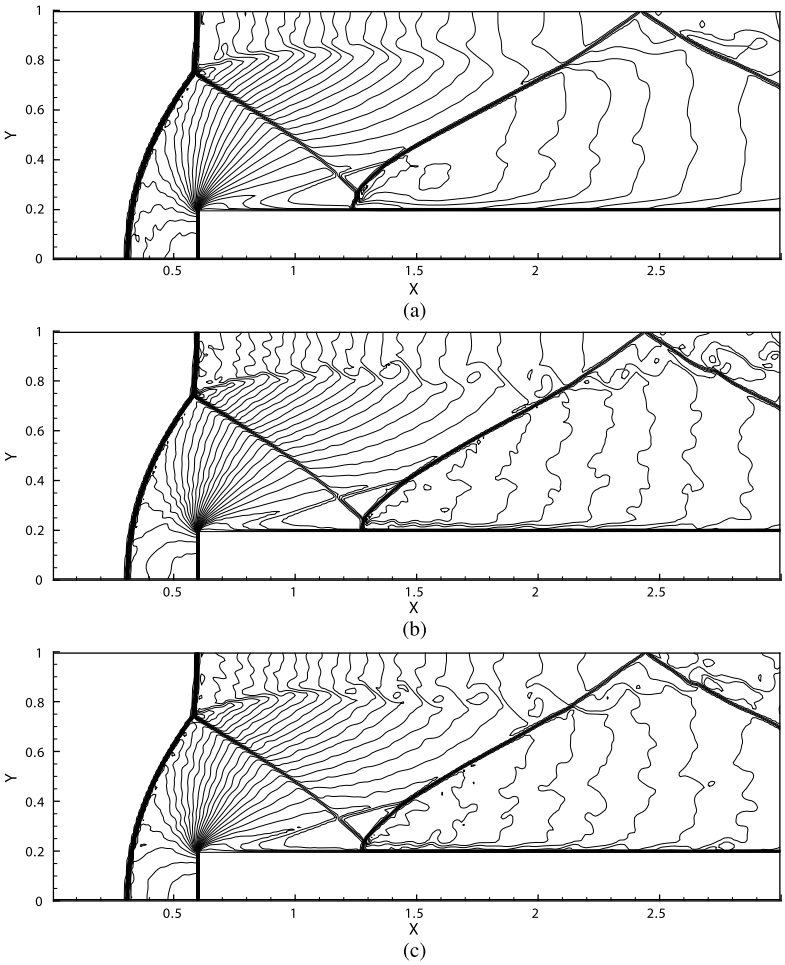

Fig. 17. Numerical results of Mach 3 step test at $t = 0.2$ on a 100×300 mesh. Displayed are the solutions of WENO-Z (a), BVD-WENOZ-THINC (b) and BVD-TENO5-THINC (c).

Acknowledgement

We gratefully acknowledge professor Denaro for providing the code to generate initial conditions in Burgers turbulence test. This work was supported in part by JSPS KAKENHI (Grant Number 15H03916).

References

[1] Y. Abe, Z.Y. Sun, F. Xiao, A note on implementation of boundary variation diminishing algorithm to high-order local polynomial-based schemes, arXiv preprint, arXiv:1605.08332.
[2] A. Aprovitola, F.M. Denaro, On the application of congruent upwind discretizations for large eddy simulations, J. Comput. Phys. 194 (2004) 329–343.
[3] G.M. Arshed, K.A. Hoffmann, Minimizing errors from linear and nonlinear weights of WENO scheme for broadband applications with shock waves, J. Comput. Phys. 246 (2013) 58–77.
[4] R. Borges, M. Carmona, B. Costa, W.S. Don, An improved weighted essentially non-oscillatory scheme for hyperbolic conservation laws, J. Comput. Phys. 227 (2008) 3191–3211.
[5] J.P. Boris, D.L. Book, Flux-corrected transport, I: SHASTA, a fluid transport algorithm that works, J. Comput. Phys. 11 (1973) 38–69.
[6] J. Casper, H.L. Atkins, A finite-volume high-order ENO scheme for two-dimensional hyperbolic systems, J. Comput. Phys. 106 (1993) 62–76.
[7] D.A. Cassidy Daniel, J.R. Edwards, M. Tian, An investigation of interface-sharpening schemes for multi-phase mixture flows, J. Comput. Phys. 228 (2009) 5628–5649.
[8] B. Cockburn, C.-W. Shu, TVB Runge–Kutta local projection discontinuous Galerkin finite element method for conservation laws II: general framework, Math. Comput. 52 (1989) 411–435.
[9] P. Colella, P.R. Woodward, The piecewise parabolic method (PPM) for gas-dynamical simulations, J. Comput. Phys. 54 (1984) 174–201.
[10] X. Deng, H. Zhang, Developing high-order weighted compact nonlinear schemes, J. Comput. Phys. 165 (2000) 22–44.
[11] M. Dumbser, O. Zanotti, R. Loubére, S. Diot, A posteriori subcell limiting of the discontinuous Galerkin finite element method for hyperbolic conservation laws, J. Comput. Phys. 278 (2014) 47–75.
[12] L. Fu, X.Y. Hu, N.A. Adams, A family of high-order targeted ENO schemes for compressible-fluid simulations, J. Comput. Phys. 305 (2016) 333–359.
[13] S.K. Godunov, A difference scheme for numerical solution of discontinuous solution of hydrodynamic equations, Math. Sb. 47 (1959) 271–306.
[14] A. Harten, High resolution schemes for hyperbolic conservation laws, J. Comput. Phys. 49 (1983) 357–393.

[15] A. Harten, B. Engquist, S. Osher, S.R. Chakravarthy, Uniformly high order accurate essentially non-oscillatory schemes III, J. Comput. Phys. 71 (1987) 231–303.
[16] A.K. Henrick, T.D. Aslam, J.M. Powers, Mapped weighted essentially nonoscillatory schemes: achieving optimal order near critical points, J. Comput. Phys. 207 (2005) 542–567.
[17] X.Y. Hu, B. Wang, N.A. Adams, An efficient low-dissipation hybrid weighted essentially non-oscillatory scheme, J. Comput. Phys. 301 (2015) 415–424.
[18] H.T. Huynh, A flux reconstruction approach to high-order schemes including discontinuous Galerkin methods, AIAA Paper 2007-4079, 2007.
[19] G. Jiang, C.W. Shu, Efficient implementation of weighted ENO schemes, J. Comput. Phys. 126 (1996) 202–228.
[20] Q. Li, P. Liu, H. Zhang, Piecewise polynomial mapping method and corresponding WENO scheme with improved resolution, Commun. Comput. Phys. 18 (2015) 1417–1444.
[21] X.D. Liu, S. Osher, T. Chan, Weighted essentially non-oscillatory schemes, J. Comput. Phys. 115 (1994) 200–212.
[22] X.L. Liu, S.H. Zhang, H.X. Zhang, C.W. Shu, A new class of central compact schemes with spectral-like resolution II: hybrid weighted nonlinear schemes, J. Comput. Phys. 284 (2015) 133–154.
[23] S.A. Moe, J.A. Rossmanith, D.C. Seal, A simple and effective high-order shock-capturing limiter for discontinuous Galerkin methods, arXiv preprint, arXiv:1507.03024.
[24] T. Nonomura, K. Kitamura, K. Fujii, A simple interface sharpening technique with a hyperbolic tangent function applied to compressible two-fluid modeling, J. Comput. Phys. 258 (2014) 95–117.
[25] S. Pirozzoli, Conservative hybrid compact-WENO schemes for shock–turbulence interaction, J. Comput. Phys. 178 (2002) 81–117.
[26] J.X. Qiu, C.W. Shu, Hermite WENO schemes and their application as limiters for Runge–Kutta discontinuous Galerkin method: one-dimensional case, J. Comput. Phys. 193 (2004) 115–135.
[27] J.X. Qiu, C.W. Shu, Runge–Kutta discontinuous Galerkin method using WENO limiters, J. Sci. Comput. 26 (2005) 907–929.
[28] Y. Ren, M. Liu, H. Zhang, A characteristic-wise hybrid compact-WENO scheme for solving hyperbolic conservation laws, J. Comput. Phys. 192 (2003) 365–386.
[29] P.L. Roe, Approximate Riemann solvers, parameter vectors, and difference schemes, J. Comput. Phys. 43 (1981) 357–372.
[30] Y.Q. Shen, G.C. Zha, Improvement of weighted essentially non-oscillatory schemes near discontinuities, Comput. Fluids 96 (2014) 1–9.
[31] C.W. Shu, High order weighted essentially non-oscillatory schemes for convection dominated problems, SIAM Rev. 51 (2009) 82–126.
[32] C.W. Shu, S. Osher, Efficient implementation of essentially non-oscillatory shock capturing schemes, J. Comput. Phys. 77 (1988) 439–471.
[33] C.W. Shu, S. Osher, Efficient implementation of essentially non-oscillatory shock capturing schemes, II, J. Comput. Phys. 83 (1989) 32–78.
[34] K.M. Shyue, F. Xiao, An Eulerian interface sharpening algorithm for compressible two-phase flow: the algebraic THINC approach, J. Comput. Phys. 268 (2014) 326–354.
[35] R. Spiteri, S.J. Ruuth, A new class of optimal high-order strong-stability-preserving time discretization methods, SIAM J. Numer. Anal. 40 (2002) 469–491.
[36] P.K. Sweby, High resolution schemes using flux-limiters for hyperbolic conservation laws, SIAM J. Numer. Anal. 21 (1984) 995–1011.
[37] V.A. Titarev, E.F. Toro, Finite-volume WENO schemes for three-dimensional conservation laws, J. Comput. Phys. 201 (2004) 238–260.
[38] E.F. Toro, Riemann Solvers and Numerical Methods for Fluid Dynamics: A Practical Introduction, third edition, Springer-Verlag, 2009.
[39] B. Van Leer, Towards the ultimate conservative difference scheme. IV. A new approach to numerical convection, J. Comput. Phys. 23 (1977) 276–299.
[40] B. Van Leer, Towards the ultimate conservative difference scheme, V. A second order sequel to Godunov's method, J. Comput. Phys. 32 (1979) 101–136.
[41] P. Woodward, P. Colella, The numerical simulation of two-dimensional fluid flow with strong shocks, J. Comput. Phys. 54 (1984) 115–173.
[42] F. Xiao, Y. Honma, T. Kono, A simple algebraic interface capturing scheme using hyperbolic tangent function, Int. J. Numer. Methods Fluids 48 (2005) 1023–1040.
[43] F. Xiao, S. Ii, C.G. Chen, Revisit to the THINC scheme: a simple algebraic VOF algorithm, J. Comput. Phys. 230 (2011) 7086–7092.
[44] S. Zalesak, Fully multidimensional flux-corrected transport algorithm for fluids, J. Comput. Phys. 31 (1979) 335–362.